**Astronomy & Astrophysics**

# Revealing the characteristics of the dark GRB 150309A: Dust extinguished or high-*z*?[*]

A. J. Castro-Tirado[1,2] , R. Gupta[3,4], S. B. Pandey[3], A. Nicuesa Guelbenzu[5], S. Eikenberry[6], K. Ackley[6], A. Gerarts[7],
A. F. Valeev[8,9] , S. Jeong[1,10], I. H. Park[10], S. R. Oates[11], B.-B. Zhang[12,13], R. Sánchez-Ramírez[1,14],
A. Martín-Carrillo[15] , J. C. Tello[1], M. Jelínek[16], Y.-D. Hu[1,17], R. Cunniffe[1], V. V. Sokolov[8], S. Guziy[1,18,19],
P. Ferrero[1], M. D. Caballero-García[1], A. K. Ror[3], A. Aryan[3,4], M. A. Castro Tirado[1], E. Fernández-García[1] ,
M. Gritsevich[20,21] , I. Olivares[1], I. Pérez-García[1], J. M. Castro Cerón[22], and J. Cepa[23]

*(Affiliations can be found after the references)*

**ABSTRACT**

*Context.* Dark gamma-ray bursts (GRBs) constitute a significant fraction of the GRB population. In this paper, we present a multi-wavelength analysis (both prompt emission and afterglow) of an intense ($3.98 \times 10^{-5}$ erg cm$^{-2}$ using *Fermi*-Gamma-Ray Burst Monitor) two-episodic GRB 150309A observed early on until ~114 days post burst. Despite the strong gamma-ray emission, no optical afterglow was detected for this burst. However, we discovered near-infrared (NIR) afterglow ($K_S$-band), ~5.2 h post burst, with the CIRCE instrument mounted at the 10.4 m Gran Telescopio Canarias (hereafter, GTC).
*Aims.* We aim to examine the characteristics of GRB 150309A as a dark burst and to constrain other properties using multi-wavelength observations.
*Methods.* We used *Fermi* observations of GRB 150309A to understand the prompt emission mechanisms and jet composition. We performed early optical observations using the BOOTES robotic telescope and late-time afterglow observations using the GTC. A potential faint host galaxy was also detected in the optical wavelength using the GTC. We modelled the potential host galaxy of GRB 150309A in order to explore the environment of the burst.
*Results.* The time-resolved spectral analysis of *Fermi* data indicates a hybrid jet composition consisting of a matter-dominated fireball and magnetic-dominated Poynting flux. The GTC observations of the afterglow revealed that the counterpart of GRB 150309A was very red, with $H - K_S > 2.1$ mag (95% confidence). The red counterpart was not discovered in any bluer filters of *Swift* UVOT/BOOTES, which would be indicative of a high redshift origin. Therefore we discarded this possibility based on multiple arguments, such as spectral analysis of the X-ray afterglow constrain $z < 4.15$ and a moderate redshift value obtained using the spectral energy distribution (SED) modelling of the potential galaxy. The broadband (X-ray to NIR bands) afterglow SED implies a very dusty host galaxy with a deeply embedded GRB (suggesting $A_V \gtrsim 35$ mag).
*Conclusions.* The environment of GRB 150309A demands a high extinction towards the line of sight. Demanding dust obscuration is the most probable origin of optical darkness as well as the very red afterglow of GRB 150309A. This result establishes GRB 150309A as the most extinguished GRB known to date.

**Key words.** techniques: photometric – gamma-ray burst: general – gamma-ray burst: individual: GRB 150309a

## 1. Introduction

Gamma-ray bursts (GRBs) are the most powerful and sudden explosions of gamma-ray radiation occurring at vast cosmological distances (Piran 2004; Kumar & Zhang 2015). These bursts can generally be categorised into two families: long duration, lasting more than two seconds, and short-duration, lasting less than two seconds (Kouveliotou et al. 1993). Long-duration GRBs are believed to originate from the collapse of massive stars (collapsar model). The core collapse of a massive star leads to the formation of a black hole or a neutron star, accompanied by the subsequent emission of a powerful and ultra-relativistic GRB jet (MacFadyen & Woosley 1999; Woosley & Bloom 2006; Heger et al. 2003; Obergaulinger & Aloy 2020). Additionally, the observational evidence of their progenitors comes from late-time multi-band observations of their afterglows and host galaxies. Some nearby long GRBs have been observed with the photometric and spectroscopic evidence of supernova signatures (Stanek et al. 2003; Cano et al. 2017), further supporting the collapsar model and a dense environment. Long-duration GRBs are often associated with regions of active star formation within their host galaxies (Bloom et al. 1998). Regarding short-duration GRBs, they are believed to originate from the merger of compact objects, such as neutron stars or black holes. The host galaxies of short-duration GRBs tend to be elliptical or lenticular galaxies, which are older and have exhausted much of their interstellar gas and dust, limiting new star formation (Perna & Belczynski 2002; Belczynski et al. 2002; Abbott et al. 2017; Goldstein et al. 2017). However, with the proliferation of observational means in recent times, there have been observations of hybrid events, including long-duration GRBs originating from mergers and short-duration GRBs of collapsar origin. These events, combining characteristics from both traditional families, challenge our classical understanding of formation and classification of GRBs (Della Valle et al. 2006; Ahumada et al. 2021; Zhang et al. 2021; Troja et al. 2022; Rastinejad et al. 2022; Yang et al. 2022; Rossi et al. 2022).

---

[*] Final (optical/ir) images+spectra are available at the CDS via anonymous ftp to cdsarc.cds.unistra.fr (130.79.128.5) or via https://cdsarc.cds.unistra.fr/viz-bin/cat/J/A+A/683/A55

There is a sub-class of GRB afterglows known as "dark bursts" for which no optical counterpart is detected in the face of deep follow-up (fainter than ∼21–22 mag) in less than 24 h after the trigger, and the number of similar sources has been increasing in the current phase of GRB research (Jakobsson et al. 2004; Greiner et al. 2011). These days, dark bursts appear to make up a significant part of the overall GRB population. From 1997 to 2021, about 66% (1526/2311) of well-localised bursts were observed with an X-ray afterglow; however, only 38% (874/2311) of the bursts were observed with an optical afterglow[1]. In some cases, optical afterglows could not be detected due to the absence of early observations (Pandey et al. 2003), but in other cases, deep and early observations revealed that true dark GRBs indeed exist and typically comprise around 25–40% of all bursts (Perley et al. 2016). In the case of GRB 150309A, an X-ray counterpart of the burst was discovered with the *Swift* X-ray telescope (XRT; Burrows et al. 2005), but no optical afterglow was discovered, in spite of a deep search using the Burst Observer and Optical Transient Exploring System (BOOTES; Castro-Tirado 2023) and Gran Telescopio Canarias (GTC) telescopes. However, observations in the near-infrared (NIR) bands using the Canarias InfraRed Camera Experiment (CIRCE) instrument mounted on the GTC telescope revealed a very red afterglow. These observations suggest that GRB 150309A belongs to the "dark bursts" sub-class.

Several methods exist in the literature to classify these dark GRBs. At the early stages of their study, GRBs without an optical afterglow were classified as dark GRBs (Groot et al. 1998). In later studies (De Pasquale et al. 2003; Jakobsson et al. 2004), the analogy between the X-ray, optical, and/or NIR afterglow properties was used for their classification. Some researchers (De Pasquale et al. 2003) used the flux ratio of optical and X-ray afterglows, while others (Jakobsson et al. 2004) used the spectral index ($\beta_{OX}$ < 0.5), obtained using optical to X-ray spectral energy distribution (SED), to classify these bursts. Another studies (van der Horst et al. 2009) suggested a more enlightened method and considered dark GRBs by $\beta_{OX}$ (joint X-ray and optical spectral index) <$\beta_X$ (X-ray spectral index) –0.5 in the framework of the fireball model.

There are many potential causes for the optical darkness of GRB afterglows. First, dark GRB afterglows could be intrinsically faint (Fynbo et al. 2001), for example, if the relativistic fireball is decelerated in a surrounding low-density medium (Sari et al. 1998). Second, the optical darkness of GRB afterglows can also likely be attributed to their high-redshift origin (Taylor et al. 1998). In this scenario, the Ly-$\alpha$ forest is anticipated to influence the optical wavelength (Lamb & Reichart 2000). The probability of optical darkness being due to a high redshift origin is low and expected for ∼10–20% of dark bursts (Perley et al. 2016). Third, in the obscuration scenario, optical darkness could be because of (i) a high column density of gas or (ii) dust in the host galaxies at larger distances such that the optical afterglow is very reddened (Fynbo et al. 2001). The last scenario is expected to be the most favoured cause for the optical darkness of GRB afterglows, as most of the host galaxies of dark bursts are detected at the optical wavelength.

The outline of the present work is as follows: In Sect. 2, we present the multi-wavelength observations and data reduction of GRB 150309A. In Sect. 3, we give the results of this work. Finally, a discussion and a brief summary and conclusion of the work are given in Sects. 4 and 5, respectively. The errors given in the paper are mentioned at the 1-$\sigma$ level unless stated otherwise.

## 2. Observations and data reduction

### 2.1. High energy gamma-ray observations

On 9 March 2015 at 22:59:50.66 UT (hereafter, $T_0$), the Gamma-Ray Burst Monitor (GBM; Meegan et al. 2009) instrument of the *Fermi* Gamma-Ray Space Mission detected a bright GRB 150309A with a $T_{90}$ duration of about 52 s (Roberts & Stanbro 2015). The GBM light curve consisted of two distinct emission episodes, the main episode followed by a soft and weak emission episode with a temporal gap of ∼200 s between (see Fig. 2). After ∼200 s (at 23:03:06 UT, $T_{sw,0}$), the Burst Alert Telescope (BAT; Barthelmy et al. 2005) instrument of the *Swift* mission also observed GRB 150309A during the second weak emission episode (Cummings et al. 2015). The mask-weighted light curve obtained using BAT observations also shows that GRB 150309A consists of two separate episodes with a $T_{90}$ duration of 242 ± 6 s (15–350 keV). The prompt emission of GRB 150309A also was independently discovered by the Konus-Wind mission (Golenetskii et al. 2015).

We retrieved photon events received by three sodium iodide (NaI) and one bismuth germanium oxide (BGO) detector (having the largest number of photon counts) of the GBM instrument onboard *Fermi*. These NaI and BGO detectors have the smallest boresight angle with respect to the GRB location. We carried out the temporal and spectral analysis of high energy gamma-ray data as described in Caballero-García et al. (2023).

### 2.2. X-ray and ultraviolet observations

The XRT instrument of the *Swift* mission started follow-up observations of the BAT localisation region at 23:05:18.2 UT (131.5 s after the BAT trigger) in order to search for X-ray afterglow. An uncatalogued counterpart (X-ray) candidate was discovered at RA, Dec = 18 h 28 m 24.81, +86 d 25′ 43.6″ (J2000) within the *Swift* BAT error circle with a 90% uncertainty radius of 1.4 arcsec[2] in the initial window timing (WT) mode exposure (Cummings et al. 2015). The position of this fading afterglow was observed up to ∼4 × 10⁵ s post BAT detection. This work utilised X-ray afterglow data products, including both light curve and spectrum, obtained from the *Swift* online repository[3] hosted and managed by the University of Leicester (Evans et al. 2007, 2009). We conducted the analysis of the X-ray afterglow spectra acquired from the *Swift* XRT using the X-Ray Spectral Fitting Package (XSPEC; Arnaud 1996). The XRT spectra were analysed within the energy range of 0.3–10 keV. For the XRT spectral analysis, we used an absorbed power-law model to explain the spectral properties of the X-ray afterglow of GRB 150309A. We considered both the photoelectric absorption from the Milky Way galaxy (phabs model in XSPEC) and the host galaxy of the GRB (zphabs model in XSPEC) along with the power-law model for the afterglow. The absorption due to our Galaxy was set as a fixed spectral parameter with a hydrogen column density of $NH_{Gal} = 9.05 \times 10^{20}$ cm$^{-2}$ (Willingale et al. 2013). However, the intrinsic absorption ($NH_z$) at the redshift value equal to two (the mean redshift $z$ value for a typical long-duration GRB) was permitted to vary freely. In addition, the photon index value of the power-law component was left to vary. We used C-Stat statistics for the spectral fitting of XRT data.

The Ultraviolet and Optical Telescope (UVOT; Roming et al. 2005) onboard *Swift* began observing the XRT localisation region 140 s after the BAT trigger in order to search for UV and

---

[1] https://www.mpe.mpg.de/~jcg/grbgen.html

[2] https://www.swift.ac.uk/xrt_positions/00634200/
[3] https://www.swift.ac.uk/

**Table 1.** Log of optical and NIR images obtained on the GRB 150309A field (top panel for the afterglow and bottom panel for the potential host galaxy).

| Date (UT, mid) | $T-T_0$ (s) | Telescope/ instrument | Filter/ grism | Exposure time (s) | Magnitude/ Upper limit |
|---|---|---|---|---|---|
| 09 Mar. 2015, 23:05:53 | 362 | 0.6 m BOOTES-2/TELMA | – | 60 | ≥18.0 |
| 09 Mar. 2015, 23:05:53 | 362 | 0.3 m BOOTES-1 | – | 60 | ≥16.5 |
| 09 Mar. 2015, 23:11:08 | 677 | 0.6 m BOOTES-2/TELMA | – | 120 | ≥20.2 |
| 10 Mar. 2015, 00:03:21 | 3810 | 0.6 m BOOTES-2/TELMA | $i$ | 5400 | ≥21.0 |
| 10 Mar. 2015, 01:22:34 | 8563 | 0.6 m BOOTES-2/TELMA | $z$ | 3600 | ≥19.2 |
| 10 Mar. 2015, 03:21:26 | 15695 | 0.6 m BOOTES-2/TELMA | $Y$ | 9300 | ≥18.0 |
| 10 Mar. 2015, 04:15 | 18909 | GTC (CIRCE) | $K_S$ | 300 | 19.28 ± 0.11 [*] |
| 10 Mar. 2015, 04:25 | 19509 | GTC (CIRCE) | $H$ | 300 | ≥21.4 [*] |
| 10 Mar. 2015, 04:35 | 20109 | GTC (CIRCE) | $J$ | 300 | ≥21.3 [*] |
| 10 Mar. 2015, 05:09 | 22149 | GTC (CIRCE) | $K_S$ | 300 | 19.50 ± 0.20 [*] |
| 03 Jul. 2015, 00:30 | 115.0625 (days) | GTC (CIRCE) | $K_S$ | 1800 | ≥21.5 [*] |
| 03 Jul. 2015, 00:40 | 115.0696 (days) | GTC (CIRCE) | $H$ | 1800 | ≥22.0 [*] |
| Date (UT, mid) | $T-T_0$ (days) | Telescope/ instrument | Filter/ grism | Exposure time (s) | Magnitude/ Upper limit |
| 19 Jul. 2015, 01:31:50 | 131.1054 | GTC (OSIRIS) | $r$ | 1800 (15 × 120 s) | 25.26 ± 0.27 |
| 24 Aug. 2015, 00:34:18 | 167.0654 | GTC (OSIRIS) | $i$ | 2160 (24 × 90 s) | 24.89 ± 0.16 |
| 25 Aug. 2015, 23:33:37 | 169.0233 | GTC (OSIRIS) | $i$ | 2160 (24 × 90 s) | 25.09 ± 0.39 |
| 07 Jul. 2016, 01:32:06 | 485.1058 | GTC (OSIRIS) | R1000B | 3600 (3 × 1200 s) | – |
| 30 Jul. 2016, 00:26:21 | 508.0600 | GTC (OSIRIS) | $g$ | 1200 (8 × 150 s) | 25.56 ± 0.27 |
| 30 Jul. 2016, 01:20:48 | 508.0979 | GTC (OSIRIS) | $i$ | 900 (10 × 90 s) | 24.80 ± 0.22 |
| 11 Mar. 2021, 05:54:10 | 2193.2879 | GTC (OSIRIS) | $z$ | 1890 (42 × 45 s) | ≥24.4 |

**Notes.** The magnitude values in different filters are uncorrected for the reddening due to our galaxy. The non-detection upper limit values are listed at $3\sigma$. The magnitudes listed are given in the AB system. The [*] marker denotes the magnitudes in the Vega system.
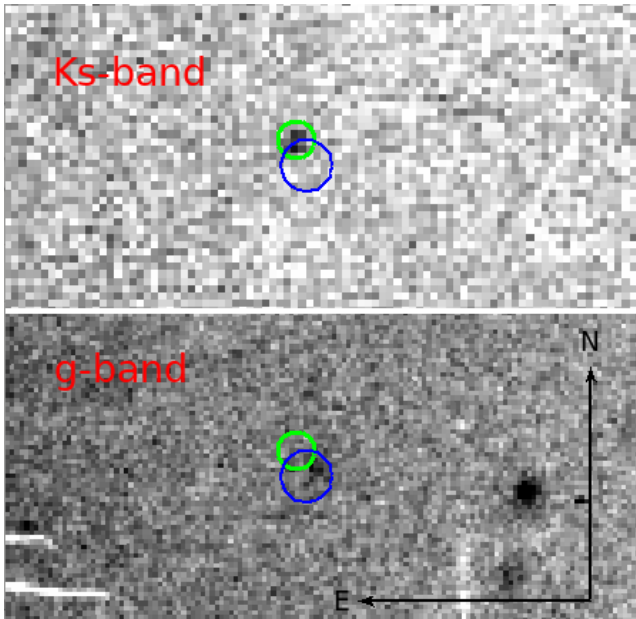


**Fig. 1.** Field of GRB 150309A. Top panel: $K_S$-band discovery image (in green circle) of the afterglow of GRB 150309A taken at the GTC (+CIRCE) in 2015. The NIR afterglow is close to the centre of the image. Bottom panel: Late-time $g$-filter image of the field observed using the GTC in July 2016. The potential host galaxy is close to the centre of the image (within the XRT error circle of radius 1.4 arcsec, shown with a blue circle). North is in the upward direction, and east is towards the left direction.

We extracted the UV afterglow data obtained by the *Swift* mission following the method described in Gupta et al. (2021).

### 2.3. Optical and near-infrared afterglow observations

For GRB 150309A, soon after the detection of an X-ray counterpart by *Swift* XRT, many ground-based optical observatories (including the BOOTES robotic telescope) started follow-up observations in order to search for the optical counterpart of GRB 150309A, although no optical afterglow (from early to late phases) candidate consistent with the BAT position was detected. Our later optical non-detections are consistent with the optical limits given by Rumyantsev et al. (2015) and Mazaeva et al. (2015).

We triggered the Target of opportunity (ToO) follow-up observations in the NIR (JHK) starting 5.0 h after the prompt discovery with the GTC equipped with the CIRCE instrument at the Spanish Observatory of La Palma. We detected a potential NIR counterpart candidate using GTC, although we could not find any afterglow emission at optical wavelengths. Additional NIR observations were made at GTC on 3 July 2015 (i.e., 114 days post burst). Table 1 displays the optical and NIR observing log of GRB 150309A. The magnitude values listed in the table are given in the AB system. The $K_S$-filter image of the GRB 150309A field taken with the GTC (+CIRCE) in 2015 is shown in Fig. 1. To determine the magnitudes from the optical and NIR frames, we utilised the DAOPHOT routine under Image Reduction and Analysis Facility (IRAF)[4].

optical afterglow. However, no credible UV or optical counterpart candidate was discovered within the *Swift* XRT detectability range (Cummings et al. 2015; Oates & Cummings 2015).

---

[4] IRAF is distributed by the NOAO, National Optical Astronomy Observatories, which are operated by USRA, the Association of Universities for Research in Astronomy, Inc., under cooperative agreement with the US National Science Foundation (NSF).

## 2.4. Search for potential host galaxy of GRB 150309A

We performed deep optical imaging in *griz* filters using the GTC telescope (see Table 1). The deeper late-time optical photometric observations were gathered on 19 July, 24 August, and 25 August 2015; 7 July and 30 July 2016; and 11 March 2021. We carried out image pre-processing, such as dark subtraction and flat fielding, using IRAF routines. Further, we performed the photometry of the cleaned GTC images using standard IRAF software. To calibrate the instrumental magnitude, we completed the field calibration using the Sloan Digital Sky Survey (SDSS) DR12 catalogue (Alam et al. 2015). At the position RA = 18:28:24.67, and Dec = +86:25:44.16 (J2000), we detected a faint galaxy with the following magnitude values $g = 25.56 \pm 0.27$, $r = 25.26 \pm 0.27$, $i = 24.80 \pm 0.22$, and $z \geq 24.4$. The position of the candidate host galaxy is consistent with the XRT position (as shown in Fig. 1). We also performed spectroscopy observations (covering the 3700–7750 Å wave range) with an exposure time of $3 \times 1200$ s on 7 July 2016 using GTC. We used standard procedures for analysing the Optical System for Imaging and low-Intermediate-Resolution Integrated Spectroscopy (OSIRIS) spectra. Table 1 shows the optical and NIR photometry of the potential host. The reported magnitude values have not been corrected for Galactic reddening. The calculated Galactic reddening value is $E(B - V) = 0.1206$ (Schlafly & Finkbeiner 2011). The potential host galaxy of GRB 150309A is shown in Fig. 1. A detailed method of host galaxy data analysis of GTC data is described in Gupta et al. (2021).

## 3. Results

### 3.1. Prompt characterisation and classification

In the following sub-sections, we present the results of the prompt analysis of GRB 150309A using high-energy observations. We explored the prompt emission mechanisms and jet composition of GRB 150309A using *Fermi* observations. Additionally, we studied the prompt properties of GRB 150309A to know the intrinsic class of the burst.

#### 3.1.1. Light curve and spectral analysis

The energy-resolved gamma-ray light curve for GRB 150309A, along with the evolution of hardness ratio (HR), is presented in Fig. 2. The light curves show two episodic emissions (main episode followed by a soft, weak episode) with a (very large) temporal gap in between (~200 s). Generally, two-episodic GRBs' prompt emission light curves to consist of three different sub-classes. They follow a soft, weak emission episode preceding the main episode; the main emission component is followed by a soft, weak emission component, or both emission episodes have comparable intensity. The second sub-class (the main emission component followed by a soft, weak emission component) is very rare (Lan et al. 2018), and GRB 150309A belongs to this rare class. The evolution of HR shows that for GRB 150309A, the first episode is harder than the subsequent episode, which is also seen from the very low signal for the second episode in the BGO 0.3–1 MeV light curve.

We performed the time-integrated and time-resolved spectral analysis using data from GBM detectors with the strongest signal: NaI 0, NaI 1, and NaI 2 (energy range 8–900 keV). We also selected the BGO detector (energy range 250–40 000 keV) closest to the GRB direction (BGO 0). We generated the custom response matrices and spectra files using the publicly
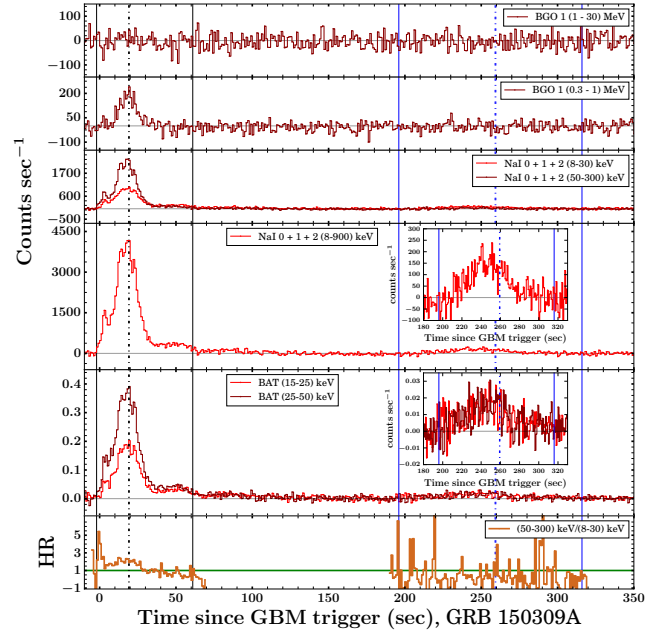
**Fig. 2.** Energy-resolved *Fermi* GBM and *Swift* BAT gamma-ray light curves of GRB 150309A: The multi-channel background-subtracted prompt emission light curve (top five panels) consists of two emission episodes with a significant temporal gap. The first and second episodes are shown with solid black and blue vertical lines, respectively. The peak times during both episodes are shown using black and blue vertical dash-dotted lines, respectively. The insets in panels four and five show a zoomed-in version of the second episode based on GBM and BAT observations. The last panel shows the evolution of the hardness ratio during both episodes. The green horizontal solid line indicates the unit value of the hardness ratio.

available `gtburst`[5] software. We used the Multi-Mission Maximum Likelihood framework (Vianello et al. 2015, `3ML`[6]) software. `3ML` serves as an interface to multiple Bayesian inference algorithms and provides posterior distributions, which help in resolving the degeneracy between different spectral model parameters. A detailed spectral analysis method is described in Caballero-García et al. (2023). The time-integrated spectra of the first episode ($T_0 -1.35$ s to $T_0 +60.00$ s) and second episode ($T_0 +215.72$ s to $T_0 +272.95$ s) were best fit by the `Band` function with the following model parameters: $E_p$ (peak energy) $= 169.53^{+5.08}_{-5.11}$, $33.07^{+5.30}_{-5.47}$ keV; $\alpha_{pt}$ (low-energy spectral index) $= -0.60^{+0.03}_{-0.03}$, $-0.59^{+0.38}_{-0.38}$; and $\beta_{pt}$ (high-energy spectral index) $= -2.86^{+0.20}_{-0.20}$, $-2.66^{+0.29}_{-0.31}$, respectively. The calculated values of $E_p$ also support the harder nature of the first episode.

Using time-resolved spectroscopy of the prompt emission of GRBs is a propitious method for exploring the emission mechanisms (thermal or non-thermal) and probing the correlations between the spectral parameters of GRBs, which are yet an open question of GRB prompt emission physics. We divided the total emission duration of the first and second episodes of GRB 150309A based on the Bayesian Block method, and we selected the energy channel from 8 keV to 900 keV in the sodium iodide detector, as having a maximum count rate (NaI 1). The Bayesian Block algorithm is considered the most acceptable method for recognizing the intrinsic intensity variation in the prompt emission light curve of GRBs (Scargle et al. 2013;

---

[5] https://fermi.gsfc.nasa.gov/ssc/data/analysis/scitools/gtburst.html

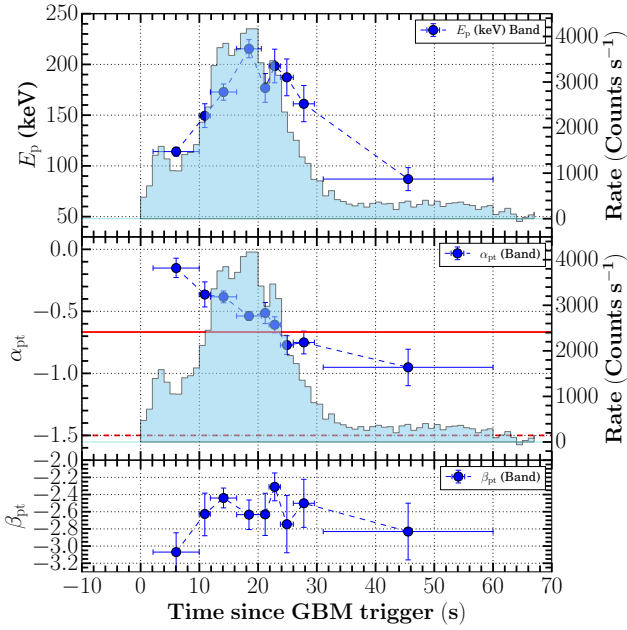[6] https://threeml.readthedocs.io/en/latest/

**Fig. 3.** Evolution of spectral parameters for GRB 150309A. Top panel: Peak energy evolving with time and following an intensity-tracking trend during the first episode. Middle panel: Evolution of low energy spectral index $\alpha_{pt}$ using *Fermi* GBM data. During the first episode, $\alpha_{pt}$ seems to follow a hard-to-soft trend. The two horizontal lines are lines of death for synchrotron fast cooling ($\alpha_{pt} = -3/2$, dotted dashed line) and synchrotron slow cooling ($\alpha_{pt} = -2/3$, solid red line). Bottom panel: Evolution of high-energy spectral index $\beta_{pt}$ using *Fermi* GBM data.

**Table 2.** Prompt emission properties of individual episodes of GRB 150309A.

| Prompt emission properties | Episode 1 | Episode 2 |
|---|---|---|
| $T_{90}$ (s) | 37.43 | 11.27 |
| $t_{mvts}$ (s) | $\sim 0.7$ | |
| HR | 1.14 | 0.20 |
| $E_p$ (keV) | $169.53^{+5.08}_{-5.11}$ | $33.07^{+5.30}_{-5.47}$ |
| $F_p$ ($10^{-7}$ erg cm$^2$ s$^{-1}$) | 7.11 | 0.27 |
| $E_{\gamma,iso}$ (erg) | $43.09 \times 10^{52}$ | $1.68 \times 10^{52}$ |
| $L_{\gamma,iso}$ (erg s$^{-1}$) | $8.72 \times 10^{52}$ | – |
| Redshift $z$ | 2.0 | |
| Spectral lag (s) | $-0.56^{+0.49}_{-0.50}$ | – |

**Notes.** The episode-wise peak fluxes are measured in the 1–10 000 keV energy range in the source frame. The terms $t_{mvts}$, HR, $E_p$, peak flux ($F_p$), $E_{\gamma,iso}$, and $L_{\gamma,iso}$ denote the minimum variability timescales, hardness ratio, peak energy, peak flux, isotropic equivalent gamma-ray energy, and isotropic equivalent gamma-ray luminosity, respectively.

Burgess 2014). At this point, we only considered the Bayesian bins with a statistical significance (S) greater than or equal to 30 in order to ensure an excellent signal-to-noise ratio for the spectral analysis. These selection criteria provided the nine spectra for the first episodes; however, no bins for the second episode fulfilled our binning criteria. We used two models (Band and cutoff power law) for time-resolved analysis. We note that most of the time-resolved spectra (5/9) for the first episode are best fitted with the Band function, and the remaining spectra for the first episode are described with the cutoff power law model. The best-fit model parameters and associated errors are given in Table A.1. The evolution of spectral parameters along with the prompt emission light curve is shown in Fig. 3. As can be seen from Fig. 3, $E_p$ changes throughout the emission episodes, resulting in spectral evolution. The $E_p$ evolution seems to follow an intensity-tracking trend for the first episode. However, the evolution of $\alpha_{pt}$ has a decreasing pattern with time. This signifies that the spectrum changes from harder to softer (a hard-to-soft trend), and the spectrum has a different origin than the synchrotron at the beginning (it exceeds the line of death for synchrotron slow cooling), but the synchrotron emission may later dominate.

We looked for the correlations between spectral parameters obtained from time-resolved spectroscopy as they play an essential role in finding the emission mechanism of the prompt emission of GRBs. We looked for the correlation between time-resolved $E_p$-flux, $\alpha_{pt}$-flux, and $E_p$-$\alpha_{pt}$ spectral parameters obtained using the Band function based on GBM observations for each temporal bin of the first episode of GRB 150309A. We found a strong correlation between the $E_p$ and the flux in the 8 keV to 30 MeV energy channels, with a Pearson coefficient ($r$) and p-value of 0.94 and $1.9 \times 10^{-4}$. We found

no correlation between the $\alpha$ of Band function and flux. Furthermore, we investigated the correlation between $E_p$ and $\alpha_{pt}$. In this case, as well, we did not find any correlation. Therefore, the first episodes of GRB 150309A have the characteristics of an "intensity-tracking" GRB (the peak energy follows the intensity-tracking pattern) similar to many multi-episodic GRBs (Li et al. 2021).

### 3.1.2. Classification of GRB 150309A

We calculated the prompt properties of GRB 150309A (see Table 2) and compared them with a large population of GRBs to know the intrinsic class of GRB 150309A. We mainly used four classifiers: spectral hardness-duration distribution, minimum variability timescale-duration distribution, spectral lag-luminosity correlation, and Amati correlation.

To find the time-integrated HR of individual episodes, we divided the counts into soft (10–50 keV) and hard (50–300 keV) energy ranges using the three brightest sodium iodide detectors of GRB 150309A. We also calculated the $T_{90}$ duration of both episodes and compared it with other two-episodic *Fermi* GRBs (with known redshift) studied by Chand et al. (2020). The spectral hardness-duration distribution diagram (see Fig. 4, top left) shows that both episodes of GRB 150309A have properties of long GRBs. The probabilities of a burst being classified as a long burst are also shown in the background of the image (obtained from Goldstein et al. 2017).

The minimum variability timescales ($t_{mvts}$) for long GRBs are typically longer than short GRBs. We calculated $t_{mvts}$ for GRB 150309A utilising the Bayesian block method on the GBM light curve in 8–900 keV. A more detailed method to determine $t_{mvts}$ is described in Vianello et al. (2018). The minimum variability timescale-duration distribution diagram for GRB 150309A (red square) along with samples of other GRBs Golkhou et al. (2015) are shown in Fig. 4 (top right). The diagram shows that GRB 150309A belongs to long GRBs. The probabilities of a burst being classified as a long burst in the sample studied by Golkhou et al. (2015) are also shown.

Further, we calculated the spectral lag for GRB 150309A following the method discussed in Caballero-García et al. (2023). We calculated the lag using prompt emission light curves
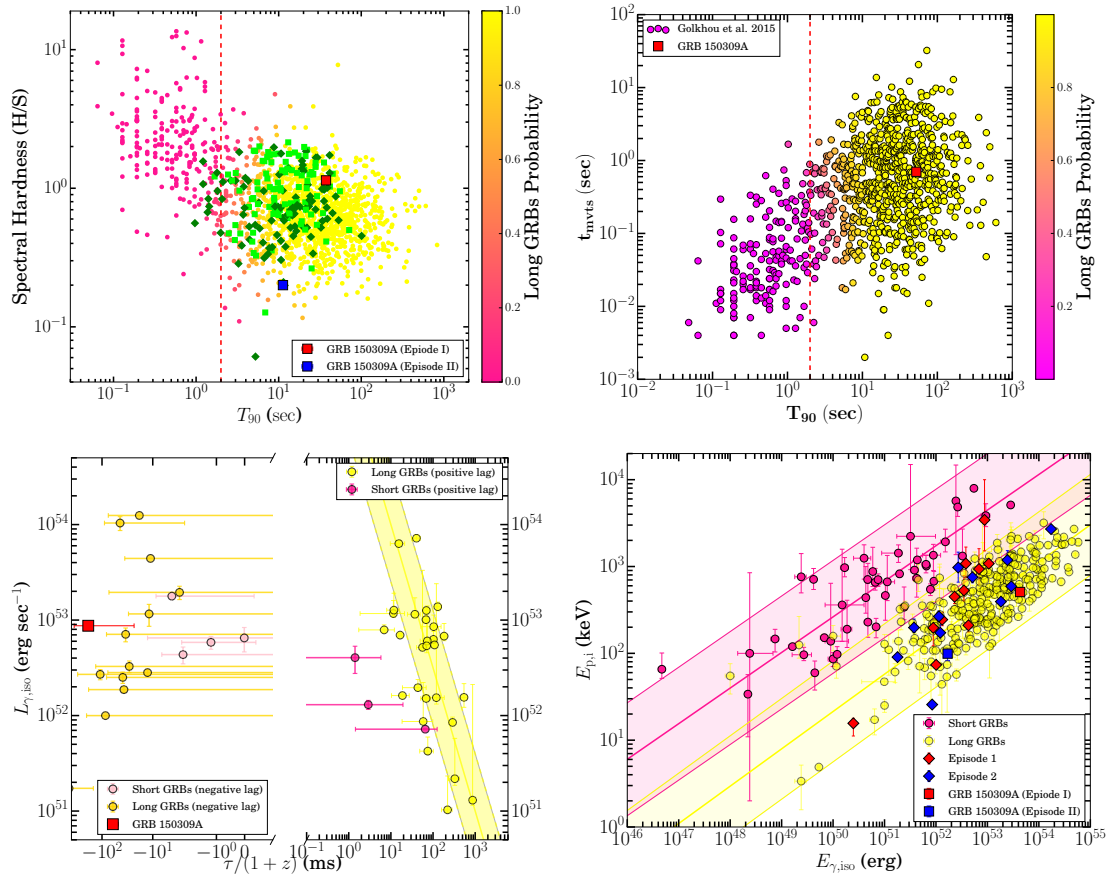
**Fig. 4.** Classification of GRB 150309A The conventional scheme of GRB classification based on the spectral hardness-duration distribution (top left), minimum variability timescale-duration distribution (top right), spectral lag-luminosity correlation (bottom left), and episode-wise Amati correlation (bottom right). The dashed lines show the boundary between long and short families of GRBs. The high-energy properties of GRB 150309A (displayed with red and blue squares) are common among long soft bursts.

($T_0 - 1.35$ s to $T_0 + 60.00$ s) in two energy ranges (15–25 keV and 50–100 keV). We obtained a negative lag for GRB 150309A (possibly due to the superposition effect). The observed negative lag indicates that the low-energy photons were observed before the high-energy photons. We also calculated the isotropic peak luminosity of GRB 150309A and plotted the spectral lag-luminosity correlation diagram (Fig. 4, bottom left) for GRB 150309A along with other samples studied by Ukwatta et al. (2010). We found that GRB 150309A does not follow the spectral lag-luminosity anti-correlation.

According to the "Amati correlation" (Amati 2006), the time-integrated peak energies corrected to the rest frame ($E_{\mathrm{p,i}}$) are correlated with the prompt emission isotropic equivalent gamma-ray energy ($E_{\gamma,\mathrm{iso}}$). This correlation was also studied and found to be valid for an episode-wise sample of GRBs (Basak & Rao 2013; Chand et al. 2020). The Amati correlation is useful for classifying the GRBs. We studied the correlation for each episode of GRB 150309A. To calculate $E_{\gamma,\mathrm{iso}}$ for both episodes, we calculated the time-integrated total energy fluence in 1–$10^4$ keV energy channels in source rest frames. In Fig. 4 (bottom right), we also show the episode-wise GRB 150309A (red and blue squares) in the Amati correlation plane along with the other data points for long GRBs and short bursts studied in Minaev & Pozanenko (2020) and Chand et al. (2020; two-episodic GRBs). We noticed that both episodes of GRB 150309A are consistent with the Amati correlation of long bursts.

### 3.2. Afterglow characteristics

In the following sub-sections, we present the results of the afterglow analysis of GRB 150309A using X-ray to NIR band observations. We used the SED analysis to examine the dark nature of GRB 150309A.

### 3.2.1. The nature of X-ray afterglow of GRB 150309A

The X-ray afterglow observations using *Swift*/XRT show a very steep decline $\alpha_{\mathrm{x1}} = -2.13^{+0.09}_{-0.09}$ from $T_{\mathrm{sw,0}} + 123$ s to $T_{\mathrm{sw,0}} + 397$ s followed by a shallower decline rate of $-1.05^{+0.03}_{-0.03}$ after $T_{\mathrm{sw,0}} + 397$ s (see Fig. A.1). We carried out *Swift* XRT spectral analysis for the temporal bins selected before and after the temporal break following Gupta et al. (2021). We calculated the spectral parameters for all the photon counting (PC) mode observations (interval after the temporal break) as the photon index value of $\Gamma_{\mathrm{XRT}} = 1.78^{+0.10}_{-0.10}$ and the intrinsic hydrogen density column $N_{\mathrm{H,z}} = 2.43^{+0.62}_{-0.57} \times 10^{22}$ cm$^{-2}$, considering $z = 2$. Our intrinsic hydrogen density column measurement shows clear evidence of excess absorption over the Galactic hydrogen column density. For the interval before the break, we froze the $N_{\mathrm{H,z}}$ from the PC mode data and calculated $\Gamma_{\mathrm{XRT}} = 1.90^{+0.05}_{-0.05}$. We also checked the evolution of photon indices from the *Swift* burst analyser page[7] and noted that photon indices do not change significantly during

---

[7] https://www.swift.ac.uk/burst_analyser/00634200/

the entire emission phase. The unavailability of obvious spectral evolution between the data before and after the break plus the large change in the temporal index rules out the possibility of relating the temporal break at $T_{sw,0}$ $+397 \pm 48.60$ s to the crossing of the cooling break frequency ($\nu_c$) across the X-ray wavelength.

The early steep decay emission observed before the break time ($<400$ s) could be interpreted as the tail (high-latitude emission) of the prompt emission. In this case, if the emission is purely non-thermal and consists of a single power-law, the temporal index can be expressed as $\alpha = 2 + \beta$ (Kumar & Panaitescu 2000). For the present burst, $\beta_1$ (X-ray spectral index during step decay phase) $= 0.90 \pm 0.05$, which results in an expected temporal index of $\sim 2.90$, is inconsistent with the observed decay ($2.13 \pm 0.09$). However, the $\alpha$–$\beta$ relation during the early steep decay phase can be explained by considering that the peak energy ($E_p$) and flux during this phase rely on the viewing angle (Rossi et al. 2011). This multi-peaked behaviour observed during the prompt emission can also cause the temporal indices to be inconsistent with the simple correlation between $\alpha$–$\beta$ during the high-latitude emission (Genet & Granot 2009).

At later times ($>400$ s), the observed temporal and spectral indices ($\alpha_2 = 1.05 \pm 0.03$, $\beta_2 = 0.78 \pm 0.10$) are dominated by non-thermal emission because of the interaction of ejecta with the ambient medium (see Sect. 3.3). To investigate the nature of the circumburst medium, interstellar medium (ISM) or wind, we applied the closure relations between the temporal and spectral index during the shallow decay phase.

Based on the evolution of cooling frequency for the afterglow of GRB 150309A, the following scenarios are possible. First, when $\nu_X < \nu_c$:

− $\alpha_{ISM} = 3\beta_2/2 = 1.17 \pm 0.15$
− $\alpha_{wind} = (3\beta_2 + 1)/2 = 1.67 \pm 0.15$

Second, when $\nu_X > \nu_c$ (both mediums are indistinguishable):

− $\alpha = (3\beta_2 - 1)/2 = 0.67 \pm 0.15$.

The case for an ISM environment with $\nu_X < \nu_c$ seems to be the best fit for our data. All these relations assume an electron spectral index of $p > 2$. The electron spectral index obtained through the closure relations is $p = 2.56 \pm 0.20$. Based on closure relations, all the cases with the wind ($\rho \propto k^{-2}$) environment seem to be completely ruled out. Further, using the calculated values of temporal ($\alpha_2 = 1.05 \pm 0.03$) and spectral ($\beta_2 = 0.78 \pm 0.10$) indices during the $\nu_X < \nu_c$ spectral regime and Eq. (1) of Martin-Carrillo et al. (2014), we computed the density profile ($k = 0$ for ISM and $k = 2$ for wind) of the environment of GRB 150309A. We obtained $k \sim -1.3$, suggesting an intermediate density between the ISM and wind ambient medium.

Additionally, we computed the value of jet kinetic energy ($E_{K,iso}$) for an ISM environment with an $\nu_X < \nu_c$ spectral regime utilising Eq. (11) of Li et al. (2018). We assumed typical micro-physical parameters (jet is due to Wiebel shocks and $\epsilon_e \approx \sqrt{\epsilon_B}$) for the afterglow of GRB 150309A, similar to other well-studied GRBs, such as $\epsilon_B$ (energy fraction in the magnetic field) $= 0.01$, $\epsilon_e$ (energy fraction in electrons) $= 0.1$, and number density $n_0 = 1$ (Panaitescu & Kumar 2002). We obtained $E_{K,iso} = 5.36 \times 10^{53}$ erg for GRB 150309A.

### 3.2.2. A potential near-infrared afterglow of GRB 150309A and its confirmation

The fact that the XRT discovered the X-ray counterpart of GRB 150309A (Cummings et al. 2015) enabled us to quickly identify a potential NIR afterglow within the XRT X-ray error box at coordinates RA (J2000) = 18 28 25.00, Dec (J2000) = +86 25 45.10 ($\pm 0\rlap{.}''4$). The source remained stable (within errors) in brightness during the CIRCE observation window, with $K_S = 19.28 \pm 0.11$ (Vega) and $K_S = 19.50 \pm 0.20$ (Vega) at the beginning and end of the observation. The object was very red (Fig. 1), and only upper limits were derived at the bluest NIR bands: $J \geq 21.3$ (Vega) and $H \geq 21.4$ (Vega). We calibrated the NIR observations utilising the Two Micron All Sky Survey (2MASS) catalogue.

In order to confirm whether the highly reddened object ($H - K_S$) $\geq 2$ is the afterglow or an extremely reddened host galaxy, a second epoch observation at GTC (+CIRCE) was conducted on 3 July 2015. No source was detected with the following upper limits, $H \geq 22.0$ (Vega) and $K_S \geq 21.5$ (Vega), implying that the afterglow faded by more than 2 mag in the $K_S$-band after 114 days. This fading behaviour confirms that the highly reddened object is the NIR afterglow of GRB 150309A.

### 3.3. Spectral energy distribution of GRB 150309A

Spectral energy distribution analysis using multi-wavelength data is very useful in constraining the location of synchrotron break frequencies and host extinction. We created the SED at $T_0$ $+5.2$ h at the time of the GTC (+CIRCE) observations (to maximise the near-simultaneous broadband coverage). We show the SED for GRB 150309A in Fig. 5. The closure relations for the X-ray afterglow support the argument that the cooling break frequency is beyond the X-ray spectral coverage ($>10$ keV) for an ISM-like ($\rho = $ constant) ambient medium and slow-cooling regime at the epoch of the SED. Our analysis suggest that no break in SED between X-ray and optical/NIR energies. Therefore, we extrapolated the unabsorbed spectral index of X-ray afterglow towards NIR wavelengths in order to calculate the extinction in the host galaxy. We noted that $K_S$ band Galactic extinction corrected detection and upper limits in $J$ and $H$ filters using the GTC telescope are situated much below the extrapolated X-ray spectral slope (see Fig. 5). Our SED analysis suggests that the host galaxy of the burst is highly extinguished, and GRB 150309A is a dark burst. We determined the $K_S$ band host extinction ($A_{K_S} = 3.60^{+0.80}_{-0.76}$ mag) utilising the X-ray to NIR SED. The calculated host extinction in the $K_S$ filter corresponds to $A_V = 34.67^{+7.70}_{-7.32}$ mag, suggesting that GRB 150309A is one of the most extinguished bursts to date. We constrained the host galaxy extinction by considering the Milky Way extinction law. We noted that such a high value of optical extinction ($A_V = 34.67^{+7.70}_{-7.32}$ mag) had been previously observed in the case of a few dark bursts, for example, GRB 051022 (Castro-Tirado et al. 2007), GRB 070306 (Jaunsen et al. 2008), GRB 080325 (Hashimoto et al. 2010), and GRB 100614A and GRB 100615A (D'Elia & Stratta 2011).

## 4. Discussion

### 4.1. GRB 150309A: a dark burst

Many possible explanations have been proposed as to why GRBs are dark. In the case of GRB 150309A, the optical non-detections up to deeper limits indicate dark behaviour following the definition proposed at the early stages of their discovery (Groot et al. 1998). In addition, we calculated the joint NIR-X-ray spectral index ($\beta_{K-X}$) for GRB 150309A (the closure relation provides support for no spectral break between NIR to X-ray and the cooling frequency lying beyond the X-ray energies) using
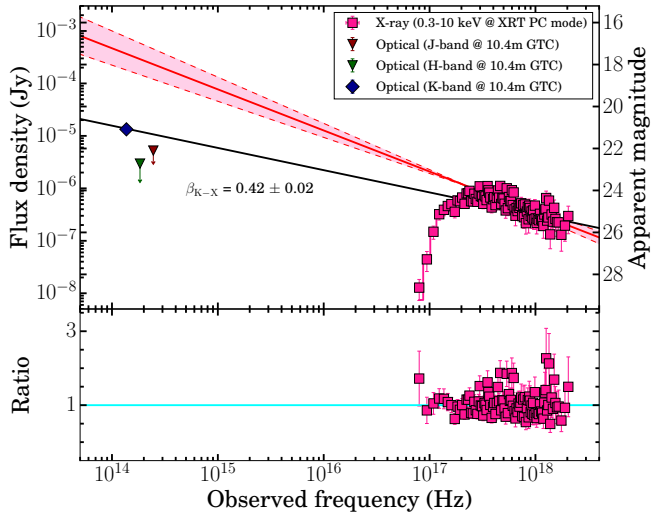
**Fig. 5.** Spectral energy distribution of GRB 150309A afterglow. Top panel: Spectral energy distribution at $T_0$ +5.2 h using the simultaneous X-ray data as well as the NIR upper limits (and the $K$-band detection) reported in this paper. The solid red line indicates the X-ray spectral slop obtained using the best-fit time-averaged PC mode spectrum, and the pink shaded region within the dashed red lines indicates the associated uncertainty with the X-ray spectral slop. The solid black line indicates the joint NIR-X-ray spectral index ($\beta_{K-X}$). The left and right sides of the $Y$-axis, representing the flux density and magnitude values, are in the AB system. Bottom panel: Ratio of X-ray observed data and best-fit model. The horizontal cyan line indicates the ratio equal to one.

**Fig. 6.** Evolution of NIR-X-ray spectral index as a function of X-ray spectral index for GRB 150309A (presented with a red square). We also show the $\beta_{OX} - \beta_X$ data points for other well-studied samples of *Swift* GRBs Melandri et al. (2012), Littlejohns et al. (2015) for comparison. The horizontal dashed black line shows the $\beta_{OX} = 0.5$.

the SED at $T_{sw,0}$ +5.2 h and noted $\beta_{K-X} = 0.42 \pm 0.02$ (see Fig. 3.3). However, we could not estimate the optical-to-X-ray spectral index ($\beta_{OX}$) at 11 h post trigger due to the unavailability of the optical observations near this epoch for GRB 150309A. The calculated value of $\beta_{K-X}$ also supports GRB 150309A being a dark burst similar to GRB 051022 (Castro-Tirado et al. 2007) and follows the definition described in Jakobsson et al. (2004). Further, we plotted the evolution of the NIR-X-ray spectral index versus the X-ray spectral index for GRB 150309A (see Fig. 6). For comparison, we also showed the $\beta_{OX} - \beta_X$ data points for other well-studied samples of *Swift* GRBs, for example, Melandri et al. (2012), Littlejohns et al. (2015). Furthermore, van der Horst et al. (2009) suggested the possible range of a joint optical-X-ray spectral slope in different possible regimes, $\beta_X - 0.5 \leq \beta_{OX} \leq \beta_X$, following the external forward shock synchrotron model. We found GRB 150309A adequately satisfies the definition of darkness suggested by van der Horst et al. (2009) in the $\nu < \nu_c$ spectral regime.

### 4.2. Origin of the optical darkness of GRB 150309A

We detected a source at the edge of the *Swift* XRT error circle (1.4 arcsec) with $K_S = 19.28 \pm 0.11$ mag (Vega) in the first set of $K_S$-band observations. We did not detect the afterglow in either the $H$ or the $J$ band data. We detected it again at $K_S = 19.50 \pm 0.20$ mag (Vega) in the second set of $K_S$ data (the magnitude difference is less than or equal to $1\sigma$, so there was apparent fading on this timescale of 20 min). The position offset of the $K_S$-band afterglow is 1.1-arcsec ± 1.5-arcsec (including 1.4-arcsec error circle from *Swift*/XRT and about 0.25-arcsec from CIRCE/2MASS astrometry), so this location is definitely in the positional uncertainty region. The clear evidence of the fading nature of the NIR source and its position being consistent
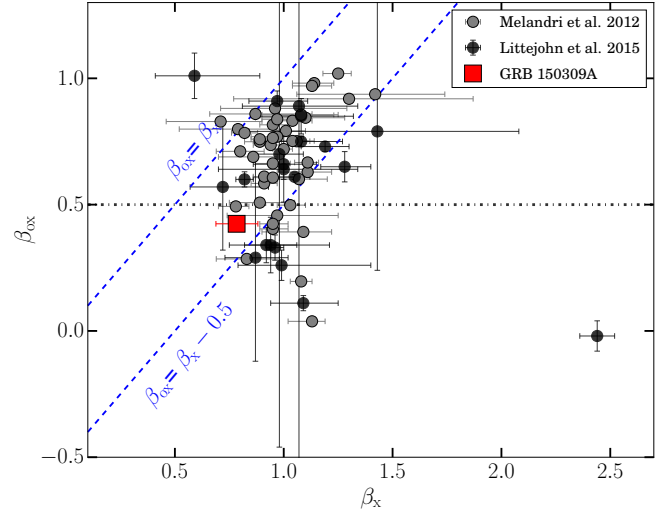
with the X-ray afterglow suggest that it is certainly the counterpart of the burst. Perhaps most interesting is the non-detection in H (bracketed in time by detection in the $K_S$-band). The 2-$\sigma$ upper limit in the $H$ band observations is $H \geq 21.4$ mag (Vega). This means that the counterpart is very red, with $H - K \geq 2.1$ mag (95% confidence). Only two scenarios are possible: (i) either GRB 150309A is deeply embedded in a very dusty host galaxy ($A_V = 34.67^{+7.70}_{-7.32}$ mag) or a very high-redshift Ly-alpha dropout ($z \geq 10$).

#### 4.2.1. Dust extinguished scenario

The observed characteristic of GRB 150309A indicates that it is positioned undoubtedly in the dark burst region of the $\beta_{OX} - \beta_X$ diagram (see Fig. 6). It is clear that the optical afterglow of GRB 150309A could not be detected because of obstruction in the line of sight. We carried out an SED analysis (at $T_{sw,0}$ +5.2 h) to determine the host extinction at NIR wavelengths. Our SED analysis suggests a $K_S$ band brightness equal to ~17.49 mag (the intrinsic afterglow brightness without any extinction obtained from the extrapolation of the unabsorbed spectral index of X-ray afterglow towards the $K_S$ band), from which we found a large host extinction at NIR wavelengths, $A_{K_S} = 3.60^{+0.80}_{-0.76}$ mag (see Sect. 3.3).

#### 4.2.2. A high redshift scenario

Based on our deep afterglow and host observations using GTC, no optical counterpart or confirmed associated host galaxy (see Sect. 4.3) was detected. Therefore, we could not calculate the exact redshift of the burst. To determine the redshift and to examine the high redshift possibility for optical darkness, we utilised prompt emission Amati correlation (the correlation between rest frame $E_p$ and isotropic gamma-ray energy). We used time-averaged spectral parameters and bolometric fluence in the source frame for different values of redshift ranging from $z = 0.1$ to $z = 10$. The Amati correlation for GRB 150309A at different redshift values is shown in Fig. 7. For comparison, we
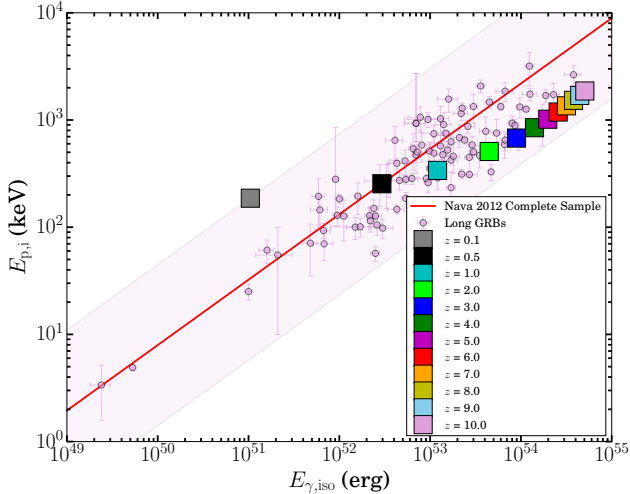
**Fig. 7.** Amati correlation for GRB 150309A. As there is no redshift measurement is available, we had to vary the redshift from 0.1 to 10. For comparison, we also show other long bursts studied by Nava et al. (2012). The solid red line shows the best-fit line, and the pink shaded band shows the associated 2-$\sigma$ uncertainty using the study of a sample of long bursts by Nava et al. (2012).

also show the other long bursts studied by Nava et al. (2012) in the figure. This analysis indicated that the isotropic gamma-ray energy of GRB 150309A is such that it would not be excessive even for $z \geq 10$. The very faint or non-detection of the afterglow in NIR, UV, and optical filters also supports a high-$z$ origin. In addition, the prompt emission duration of GRB 150309A would be ~5 s in the source frame at $z \geq 10$, which is consistent with a long GRB.

However, the high redshift origin of GRB 150309A is challenged based on the following argument: Considering a high redshift origin of GRB 150309A, the soft X-ray photons in the source frame would be shifted out of the XRT energy coverage (0.3–10 keV). Therefore, even a large column density in the source would result in little attenuation. We utilised the X-ray afterglow spectrum to constrain the redshift of GRB 150309A. We fitted the X-ray PC mode spectral data and derived column density (observer frame) considering $z = 0$. The measured column density is higher than that of the Galactic column density, and this excess column density is useful to estimate the limit on $z$. We used the following equation to constrain the limit on $z$ Grupe & Nousek (2007):

$$\log(1 + z) < 1.3 - 0.5 \log_{10}(1 + \Delta N_H), \tag{1}$$

where $\Delta N_H$ represents the difference between the column density measured considering $z = 0$ ($N_H \sim 23.06 \times 10^{20}$ cm$^{-2}$) and the Galactic column density ($N_H \sim 9.05 \times 10^{20}$ cm$^{-2}$), taken from Willingale et al. (2013). The above equation indicates that GRB 150309A has a redshift value $z < 4.15$.

### 4.3. Nature of the potential host galaxy of GRB 150309A

Deeper observations searching the host of GRB 150309A found a potential host with an angular separation of ~1.1″ from the NIR afterglow position (see Sect. 2.4). The potential host is a faint ($r \sim 25.26 \pm 0.27$ mag) one with a typical $g - i$ colour measured for galaxies at moderate redshift values detected in the optical bands (see Table 1). The observed spectrum of the potential host galaxy taken using GTC was very noisy, and there is no emission-like feature up to $z = 1.08$. Consequently, this nullified the low-

redshift possibility (the non-detection of UV emission also invalidates the low redshift possibility). So we executed the SED modelling of the potential galaxy of GRB 150309A utilising photometric data and `Prospector` software. A python-based stellar population code, `Prospector` was developed for the host galaxy SED modelling using both photometric and spectroscopic observations (Leja et al. 2017; Johnson et al. 2021). In order to model the observed data, `Prospector` applies a library of Flexible Stellar Population Synthesis (FSPS) models (Conroy et al. 2009). We used the dynamic nested sampling fitting routine `dynesty` on the observed photometry of the potential host galaxy and calculated the posterior distributions of host galaxy parameters. To determine the stellar population properties of the potential host galaxy, we used the `parametric_sfh` model. This model enabled us to calculate several key host properties, including the stellar mass formed ($M_\star$) in solar mass units, host galaxy age ($t$), stellar metallicity ($\log Z/Z_\odot$), dust attenuation ($A_V$), and the star-formation timescale ($\tau$). In our SED analysis, we used these host galaxy model parameters as free variables. A detailed description of the host galaxy SED modelling method is provided in Gupta et al. (2022). Due to the limited number of data points, we also included the limiting magnitude values of $z$, $H$, and $K_S$ filters for the SED analysis. We set redshift as a free parameter in order to constrain the photometric redshift of the potential host galaxy. Figures 8 and A.2 show the SED fitting and a corresponding corner plot of the potential host galaxy of GRB 150309A, respectively. We determined the following parameters using SED modelling: stellar mass formed ($M_\star$) = $10.66^{+0.44}_{-0.54}$; stellar metallicity ($\log Z/Z_\odot$) = $-2.27^{+1.12}_{-0.83}$; age of the galaxy ($t$) = $5.80^{+4.77}_{-3.66}$; dust attenuation in rest frame ($A_V$) = $0.97^{+0.34}_{-0.37}$ mag; and star formation timescale ($\tau$) = $1.68^{+0.82}_{-0.83}$. Considering the redshift 1.88 obtained from the SED modelling, we calculated the physical offset ~9.5 kpc between the centre of the potential host galaxy and the NIR afterglow position. The measured physical distance is very large compared to those typically observed for long GRBs, suggesting that the galaxy might not be related to GRB 150309A. To further explore the nature of the potential galaxy, we calculated the coincidence probability of the candidate galaxy following the method described in Bloom et al. (2002). Using the measured brightness of the galaxy in the $r$-band and the observed offset values, we derived a chance alignment ($P_{cc}$) of about 5%. The derived $P_c$ value is small but still significantly high, indicating the candidate galaxy to be the host. In the literature, authors have used a diverse range of $P_{cc}$ values, that is, ~1–10%, to establish the association of faint galaxies with such transients. For example, Bloom et al. (2002), Berger (2010), O'Connor et al. (2022) used $P_{cc} < 10\%$, Fong et al. (2013) used $P_{cc} < 5\%$, and Tunnicliffe et al. (2014) used 1–2% to identify if a galaxy is related to an afterglow or not. In light of the above analysis, it is hard to decipher whether the observed candidate galaxy is the host of GRB 150309A.

## 5. Conclusions

We investigated detailed prompt emission properties of GRB 150309A detected by *Swift* and *Fermi*. The high-energy light curve of GRB 150309A consists of a rarely observed two-episodic emission phase intersected by a quiescent gap where the first (main) episode was brighter while the second episode was fainter and softer. Our episode-wise time-averaged as well as time-resolved spectral analysis of high-energy observations of GRB 150309A exhibited intensity-tracking peak energy $E_p$ evolution. The evolution of the low-energy index ($\alpha_{pt}$) of the
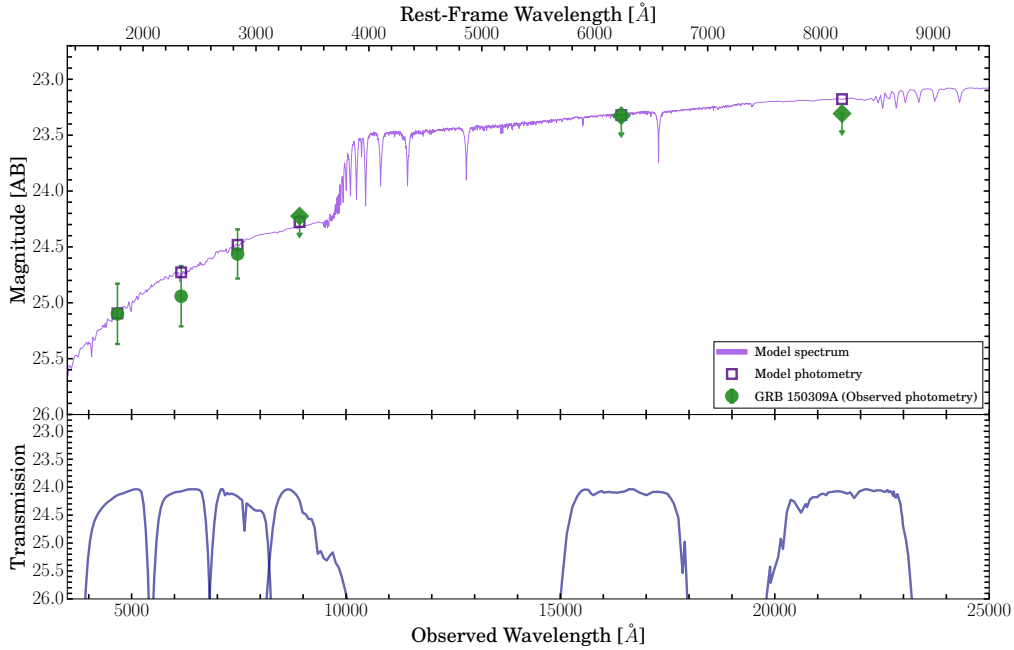
**Fig. 8.** Spectral energy distribution modelling of the potential host galaxy (from the $g$-band to the $K_S$ band) of GRB 150309A using `Prospector` software. The SED fitting shows no evidence of internal reddening. The bottom plot shows the transmission curves of the corresponding filters.

`Band` function overshot the synchrotron limits in early temporal bins of the first episode, posing challenges for the thin shell synchrotron origin and demands for photospheric contribution; however, more complex synchrotron emission models (such as synchrotron emission in the decaying magnetic field or time-dependent cooling of electrons) may produce harder $\alpha_{pt}$. Our detailed time-resolved spectral analysis of high-energy data helped us to understand the radiation physics and jet composition of GRB 150309A. The evolution of $\alpha_{pt}$ indicates a hybrid jet composition consisting of a matter-dominated fireball and magnetic-dominated Poynting flux. Considering the value of $E_{\gamma,iso}$ for an assumed value of $z = 2$, and derived value of $E_{K,iso}$, we constrained the radiative efficiency ($\eta = E_{\gamma,iso}/(E_{\gamma,iso}+E_{K,iso})$) as <0.4, which is similar to what has been found in cases of other long GRBs.

Detection of the very red afterglow is crucial to exploring the early universe, as it serves as a probe to look for very high redshifts or as a test bed for studying dusty environments surrounding GRBs. In this work, we apprised the discovery of a very red counterpart ($K_S$-band) of GRB 150309A ~5.2 h post burst with the CIRCE instrument mounted on the GTC, but it was not detected in any bluer filters of *Swift* UVOT/BOOTES, suggesting a very high redshift origin. However, our present analysis discarded this possibility based on a few arguments, including spectral analysis of X-ray afterglow, constraining $z < 4.15$; SED modelling of the potential nearby galaxy constraining moderate redshift values; and offset analysis between the centroid of the potential host to the location of the afterglow. Furthermore, we also performed SED modelling of the potential host galaxy. Our results demand a relatively lower value of extinction and redshift along with typical physical parameters with a rather large physical offset from the galaxy's centre. The considerable difference between the $A_V$ values obtained from the host galaxy SED modelling and those estimated from afterglow SED analysis of GRB 150309A is indicative of local dust surrounding the progenitor or anomalous extinction within the host galaxy, as described in Perley et al. (2009, 2013). Based on our analysis of

the potential host, it is hard to decipher whether the observed candidate galaxy is the host of GRB 150309A.

Our analysis of the afterglow SED shows that significant reddening is required to describe the observed $K_S$ band (NIR) afterglow of GRB 150309A, assuming the cooling frequency of the external synchrotron model is beyond the optical, NIR, and X-ray frequencies. Following this method, we calculated the $K_S$ band host reddening $(A_{K_S}) = 3.60^{+0.80}_{-0.76}$ mag, which is equivalent to $A_V = 34.67^{+7.70}_{-7.32}$ mag. Our analysis also indicates that GRB 150309A is one of the most intense dark GRBs detected so far. Our results suggest that the environment of GRB 150309A demands a high extinction towards the line of sight. Hence, dust obscuration is the most probable reason for the optical darkness of GRB 150309A.

The synergy between state-of-the-art NIR cameras such as CIRCE and the largest diameter optical telescope available so far (the GTC), along with the recently launched *James Webb* Space Telescope, makes an ideal combination for studying the population of dark GRBs to a great extent and determining if extinction in the host galaxy or very high redshift is the reason for a significant fraction of the afterglows being beyond the reach of optical telescopes in about 20% of events (Greiner et al. 2011; Tanvir et al. 2008; D'Elia & Stratta 2011). Furthermore, the community is developing several larger optical telescopes, for example, the Extremely Large Telescope (ELT) and the Thirty Meter Telescope (TMT). Our study provides insights for future observations of similar fainter afterglows of dark GRBs using upcoming larger telescopes (Pandey 2013).

# References

Abbott, B. P., Abbott, R., Abbott, T. D., et al. 2017, ApJ, 848, L13
Ahumada, T., Singer, L. P., Anand, S., et al. 2021, Nat. Astron., 5, 917
Alam, S., Albareti, F. D., Allende Prieto, C., et al. 2015, ApJS, 219, 12
Amati, L. 2006, MNRAS, 372, 233
Arnaud, K. A. 1996, in Astronomical Data Analysis Software and Systems V, eds. G. H. Jacoby, & J. Barnes, ASP Conf. Ser., 101, 17
Barthelmy, S. D., Barbier, L. M., Cummings, J. R., et al. 2005, Space Sci. Rev., 120, 143
Basak, R., & Rao, A. R. 2013, MNRAS, 436, 3082
Belczynski, K., Bulik, T., & Rudak, B. 2002, ApJ, 571, 394
Berger, E. 2010, ApJ, 722, 1946
Bloom, J. S., Djorgovski, S. G., Kulkarni, S. R., & Frail, D. A. 1998, ApJ, 507, L25
Bloom, J. S., Kulkarni, S. R., & Djorgovski, S. G. 2002, AJ, 123, 1111
Burgess, J. M. 2014, MNRAS, 445, 2589
Burrows, D. N., Hill, J. E., Nousek, J. A., et al. 2005, Space Sci. Rev., 120, 165
Caballero-García, M. D., Gupta, R., Pandey, S. B., et al. 2023, MNRAS, 519, 3201
Cano, Z., Wang, S.-Q., Dai, Z.-G., & Wu, X.-F. 2017, Adv. Astron., 2017, 8929054
Castro-Tirado, A. J. 2023, Nat. Astron., 7, 1136
Castro-Tirado, A. J., Bremer, M., McBreen, S., et al. 2007, A&A, 475, 101
Chand, V., Banerjee, A., Gupta, R., et al. 2020, ApJ, 898, 42
Conroy, C., Gunn, J. E., & White, M. 2009, ApJ, 699, 486
Cummings, J. R., Barthelmy, S. D., Page, K. L., Palmer, D. M., & Ukwatta, T. N. 2015, GCN, 17553, 1
D'Elia, V., & Stratta, G. 2011, A&A, 532, A48
Della Valle, M., Chincarini, G., Panagia, N., et al. 2006, Nature, 444, 1050
De Pasquale, M., Piro, L., Perna, R., et al. 2003, ApJ, 592, 1018
Evans, P. A., Beardmore, A. P., Page, K. L., et al. 2007, A&A, 469, 379
Evans, P. A., Beardmore, A. P., Page, K. L., et al. 2009, MNRAS, 397, 1177
Fong, W., Berger, E., Chornock, R., et al. 2013, ApJ, 769, 56
Fynbo, J. U., Gorosabel, J., Dall, T. H., et al. 2001, A&A, 373, 796
Genet, F., & Granot, J. 2009, MNRAS, 399, 1328
Goldstein, A., Veres, P., Burns, E., et al. 2017, ApJ, 848, L14
Golenetskii, S., Aptekar, R., Frederiks, D., et al. 2015, GCN, 17566, 1
Golkhou, V. Z., Butler, N. R., & Littlejohns, O. M. 2015, ApJ, 811, 93
Greiner, J., Krühler, T., Klose, S., et al. 2011, A&A, 526, A30
Groot, P. J., Galama, T. J., van Paradijs, J., et al. 1998, ApJ, 493, L27
Grupe, D., Nousek, J. A., vanden Berk, D. E., , et al. 2007, AJ, 133, 2216
Gupta, R., Oates, S. R., Pandey, S. B., et al. 2021, MNRAS, 505, 4086
Gupta, R., Pandey, S. B., Kumar, A., et al. 2022, JApA, 43, 82
Hashimoto, T., Ohta, K., Aoki, K., et al. 2010, ApJ, 719, 378
Heger, A., Fryer, C. L., Woosley, S. E., Langer, N., & Hartmann, D. H. 2003, ApJ, 591, 288
Jakobsson, P., Hjorth, J., Fynbo, J. P. U., et al. 2004, ApJ, 617, L21
Jaunsen, A. O., Rol, E., Watson, D. J., et al. 2008, ApJ, 681, 453
Johnson, B. D., Leja, J., Conroy, C., & Speagle, J. S. 2021, ApJS, 254, 22
Kouveliotou, C., Meegan, C. A., Fishman, G. J., et al. 1993, ApJ, 413, L101
Kumar, P., & Panaitescu, A. 2000, ApJ, 541, L51
Kumar, P., & Zhang, B. 2015, Phys. Rep., 561, 1
Lamb, D. Q., & Reichart, D. E. 2000, ApJ, 536, 1
Lan, L., Lü, H.-J., Zhong, S.-Q., et al. 2018, ApJ, 862, 155
Leja, J., Johnson, B. D., Conroy, C., van Dokkum, P. G., & Byler, N. 2017, ApJ, 837, 170
Li, L., Wu, X.-F., Lei, W.-H., et al. 2018, ApJS, 236, 26
Li, L., Ryde, F., Pe'er, A., Yu, H.-F., & Acuner, Z. 2021, ApJS, 254, 35
Littlejohns, O. M., Butler, N. R., Cucchiara, A., et al. 2015, MNRAS, 449, 2919

MacFadyen, A. I., & Woosley, S. E. 1999, ApJ, 524, 262
Martin-Carrillo, A., Hanlon, L., Topinka, M., et al. 2014, A&A, 567, A84
Mazaeva, E., Inasaridze, R., Makandarashvili, S., et al. 2015, GCN, 17570, 1
Meegan, C., Lichti, G., Bhat, P. N., et al. 2009, ApJ, 702, 791
Melandri, A., Sbarufatti, B., D'Avanzo, P., et al. 2012, MNRAS, 421, 1265
Minaev, P. Y., & Pozanenko, A. S. 2020, MNRAS, 492, 1919
Nava, L., Salvaterra, R., Ghirlanda, G., et al. 2012, MNRAS, 421, 1256
Oates, S. R., & Cummings, J. R. 2015, GCN, 17559, 1
Obergaulinger, M., & Aloy, M. Á. 2020, MNRAS, 492, 4613
O'Connor, B., Troja, E., Dichiara, S., et al. 2022, MNRAS, 515, 4890
Panaitescu, A., & Kumar, P. 2002, ApJ, 571, 779
Pandey, S. B. 2013, JApA, 34, 157
Pandey, S. B., Anupama, G. C., Sagar, R., et al. 2003, A&A, 408, L21
Perley, D. A., Cenko, S. B., Bloom, J. S., et al. 2009, AJ, 138, 1690
Perley, D. A., Levan, A. J., Tanvir, N. R., et al. 2013, ApJ, 778, 128
Perley, D. A., Krühler, T., Schulze, S., et al. 2016, ApJ, 817, 7
Perna, R., & Belczynski, K. 2002, ApJ, 570, 252
Piran, T. 2004, Rev. Mod. Phys., 76, 1143
Rastinejad, J. C., Gompertz, B. P., Levan, A. J., et al. 2022, Nature, 612, 223
Roberts, O. J., & Stanbro, M. 2015, GCN, 17561, 1
Roming, P. W. A., Kennedy, T. E., Mason, K. O., et al. 2005, Space Sci. Rev., 120, 95
Rossi, A., Schulze, S., Klose, S., et al. 2011, A&A, 529, A142
Rossi, A., Rothberg, B., Palazzi, E., et al. 2022, ApJ, 932, 1
Rumyantsev, V., Antoniuk, K., Mazaeva, E., & Pozanenko, A. 2015, GCN, 17565, 1
Sari, R., Piran, T., & Narayan, R. 1998, ApJ, 497, L17
Scargle, J. D., Norris, J. P., Jackson, B., & Chiang, J. 2013, ArXiv e-prints [arXiv:1304.2818]
Schlafly, E. F., & Finkbeiner, D. P. 2011, ApJ, 737, 103
Stanek, K. Z., Matheson, T., Garnavich, P. M., et al. 2003, ApJ, 591, L17
Tanvir, N. R., Levan, A. J., Rol, E., et al. 2008, MNRAS, 388, 1743
Taylor, G. B., Frail, D. A., Kulkarni, S. R., et al. 1998, ApJ, 502, L115
Troja, E., Fryer, C. L., O'Connor, B., et al. 2022, Nature, 612, 228
Tunnicliffe, R. L., Levan, A. J., Tanvir, N. R., et al. 2014, MNRAS, 437, 1495
Ukwatta, T. N., Stamatikos, M., Dhuga, K. S., et al. 2010, ApJ, 711, 1073
van der Horst, A. J., Kouveliotou, C., Gehrels, N., et al. 2009, ApJ, 699, 1087
Vianello, G., Lauer, R. J., Younk, P., et al. 2015, ArXiv e-prints [arXiv:1507.08343]
Vianello, G., Gill, R., Granot, J., et al. 2018, ApJ, 864, 163
Willingale, R., Starling, R. L. C., Beardmore, A. P., Tanvir, N. R., & O'Brien, P. T. 2013, MNRAS, 431, 394
Woosley, S. E., & Bloom, J. S. 2006, ARA&A, 44, 507
Yang, J., Ai, S., Zhang, B.-B., et al. 2022, Nature, 612, 232
Zhang, B. B., Liu, Z. K., Peng, Z. K., et al. 2021, Nat. Astron., 5, 911

[1] Instituto de Astrofísica de Andalucía (IAA-CSIC), Glorieta de la Astronomía s/n, 18008 Granada, Spain
e-mail: ajct@iaa.es

[2] Departamento de Ingeniería de Sistemas y Automática, Escuela de Ingenierías, Universidad de Málaga, C. Dr. Ortiz Ramos sn, 29071 Málaga, Spain

[3] Aryabhatta Research Institute of Observational Sciences (ARIES), Manora Peak, Nainital 263002, India
e-mail: rahulbhu.c157@gmail.com

[4] Department of Physics, Deen Dayal Upadhyaya Gorakhpur University, Gorakhpur 273009, India

[5] Thüringer Landessternwarte Tautenburg, Sternwarte 5, 07778 Tautenburg, Germany

[6] Department of Astronomy, University of Florida, Bryant Space Science Center, Gainesville, FL 32611, USA

[7] Grantecan, Santa Cruz de la Palma, Tenerife, Spain

[8] Special Astrophysical Observatory of Russian Academy of Sciences, Nizhniy Arkhyz 369167, Russia

[9] Crimean Astrophysical Observatory, Russian Academy of Sciences, Nauchnyi 298409, Russia

[10] Institute for Science and Technology in Space, SungKyunKwan University, Suwon 16419, Korea

[11] School of Physics and Astronomy, University of Birmingham, Birmingham B15 2TT, UK

[12] School of Astronomy and Space Science, Nanjing University, Nanjing 210093, PR China

[13] Key Laboratory of Modern Astronomy and Astrophysics, Nanjing University, Ministry of Education, Nanjing 210093, PR China

[14] INAF, Istituto di Astrofisica e Planetologia Spaziali, Via Fosso del Cavaliere 100, 00133 Rome, Italy

[15] School of Physics, O'Brien Centre for Science North, University College Dublin, Belfield, Dublin 4, Ireland

[16] Astronomical Institute of the Czech Academy of Sciences (ASU-CAS), Fričova 298, 251 65 Ondřejov, Czech Republic

[17] Universidad de Granada, Facultad de Ciencias Campus Fuentenueva s/n, 18071 Granada, Spain

[18] Nikolaev National University, Nikolska 24, Nikolaev 54030, Ukraine

[19] Nikolaev Astronomical Observatory, Nikolaev 54030, Ukraine

[20] Department of Physics, University of Helsinki, Gustav Hällströmin katu 2, 00014 Helsinki, Finland

[21] Institute of Physics and Technology, Ural Federal University, Mira Street 19, 620002 Ekaterinburg, Russia

[22] European Space Astronomy Centre (ESA-ESAC), Camino bajo del Castillo, s/n, Villafranca del Castillo, 28692 Villanueva de la Cañada, Madrid, Spain

[23] Instituto de Astrofísica de Canarias, Via Láctea s/n, La Laguna, Tenerife, Spain

# Appendix A: Additional material

**Table A.1.** Time-resolved spectral fitting of the first episode of GRB 150309A using `Band` and `CPL` models. The listed flux values are estimated in 8 keV–40 MeV.

| $T_{start}$ (s) | $T_{stop}$ (s) | Significance | $\alpha_{pt}$ | $\beta_{pt}$ | $E_p$ (keV) | (Flux $\times 10^{-06}$) | $DIC_{Band}$ | $\Gamma_{CPL}$ | $E_c$ (keV) | (Flux $\times 10^{-06}$) | $DIC_{CPL}$ | $\Delta$ DIC |
|---|---|---|---|---|---|---|---|---|---|---|---|---|
| 2.119 | 9.975 | 40.59 | $-0.15^{+0.08}_{-0.08}$ | $-3.07^{+0.22}_{-0.23}$ | $114.09^{+4.34}_{-4.54}$ | 0.58 | 4572.74 | $-0.23^{+0.07}_{-0.07}$ | $68.02^{+4.52}_{-4.67}$ | 0.49 | 4570.91 | 1.83 |
| 9.975 | 11.875 | 33.09 | $-0.36^{+0.10}_{-0.10}$ | $-2.63^{+0.24}_{-0.25}$ | $149.37^{+11.85}_{-11.59}$ | 1.37 | 2593.98 | $-0.48^{+0.08}_{-0.08}$ | $112.10^{+11.79}_{-12.12}$ | 1.02 | 2593.37 | 0.61 |
| 11.875 | 16.349 | 74.58 | $-0.38^{+0.05}_{-0.05}$ | $-2.44^{+0.12}_{-0.11}$ | $172.78^{+7.96}_{-8.02}$ | 2.8 | 3898.49 | $-0.50^{+0.03}_{-0.03}$ | $134.78^{+6.73}_{-6.69}$ | 1.87 | 3922.39 | -23.9 |
| 16.349 | 20.547 | 82.42 | $-0.54^{+0.04}_{-0.04}$ | $-2.63^{+0.17}_{-0.17}$ | $215.39^{+8.98}_{-8.90}$ | 3.12 | 3731.73 | $-0.60^{+0.03}_{-0.03}$ | $168.88^{+8.03}_{-8.17}$ | 2.37 | 3741.33 | -9.6 |
| 20.547 | 21.861 | 33.15 | $-0.51^{+0.08}_{-0.09}$ | $-2.63^{+0.25}_{-0.25}$ | $176.76^{+14.22}_{-14.07}$ | 1.95 | 2035.34 | $-0.60^{+0.07}_{-0.07}$ | $142.79^{+16.30}_{-16.29}$ | 1.47 | 2036.18 | -0.84 |
| 21.861 | 23.799 | 48.52 | $-0.61^{+0.06}_{-0.06}$ | $-2.31^{+0.16}_{-0.16}$ | $198.38^{+16.64}_{-16.56}$ | 3.15 | 2656.74 | $-0.71^{+0.05}_{-0.05}$ | $185.58^{+17.54}_{-17.42}$ | 1.93 | 2671.61 | -14.87 |
| 23.799 | 25.994 | 34.11 | $-0.77^{+0.08}_{-0.07}$ | $-2.75^{+0.34}_{-0.33}$ | $187.26^{+18.09}_{-18.14}$ | 1.3 | 2701.82 | $-0.81^{+0.06}_{-0.06}$ | $169.40^{+21.18}_{-21.11}$ | 1.03 | 2700.68 | 1.14 |
| 25.994 | 29.582 | 29.29 | $-0.75^{+0.09}_{-0.09}$ | $-2.50^{+0.28}_{-0.28}$ | $161.17^{+18.08}_{-17.65}$ | 0.87 | 3385.32 | $-0.82^{+0.08}_{-0.08}$ | $157.01^{+23.98}_{-24.01}$ | 0.6 | 3387.92 | -2.6 |
| 31.088 | 60.001 | 18.84 | $-0.95^{+0.15}_{-0.15}$ | $-2.83^{+0.33}_{-0.33}$ | $87.04^{+11.25}_{-11.39}$ | 0.12 | 6215.44 | $-1.03^{+0.12}_{-0.12}$ | $100.06^{+21.49}_{-21.18}$ | 0.09 | 6212.99 | 2.45 |
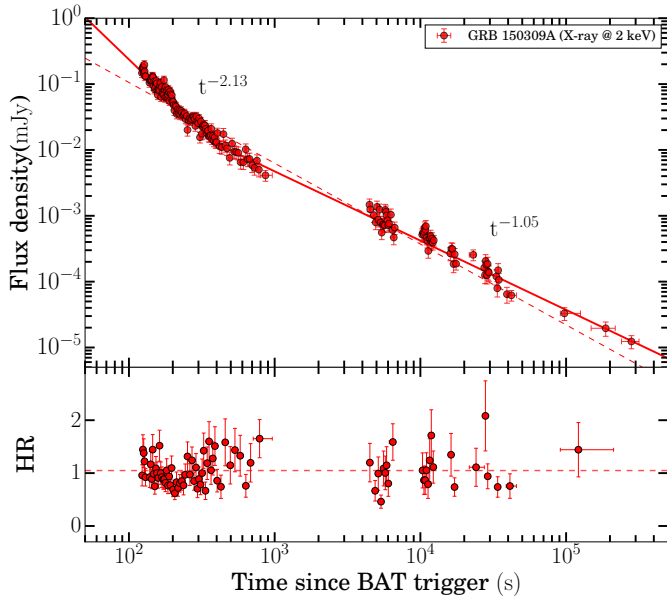


**Fig. A.1.** X-ray flux light curve of GRB 150309A. Top panel: XRT flux light curves at the 2 keV energy range. The light curve has been fitted with power-law and broken power-law (best fit) models. Bottom panel: Evolution of hardness ratio in the XRT energy channel. The dashed vertical red line indicates the mean value of the hardness ratio for GRB 150309A.
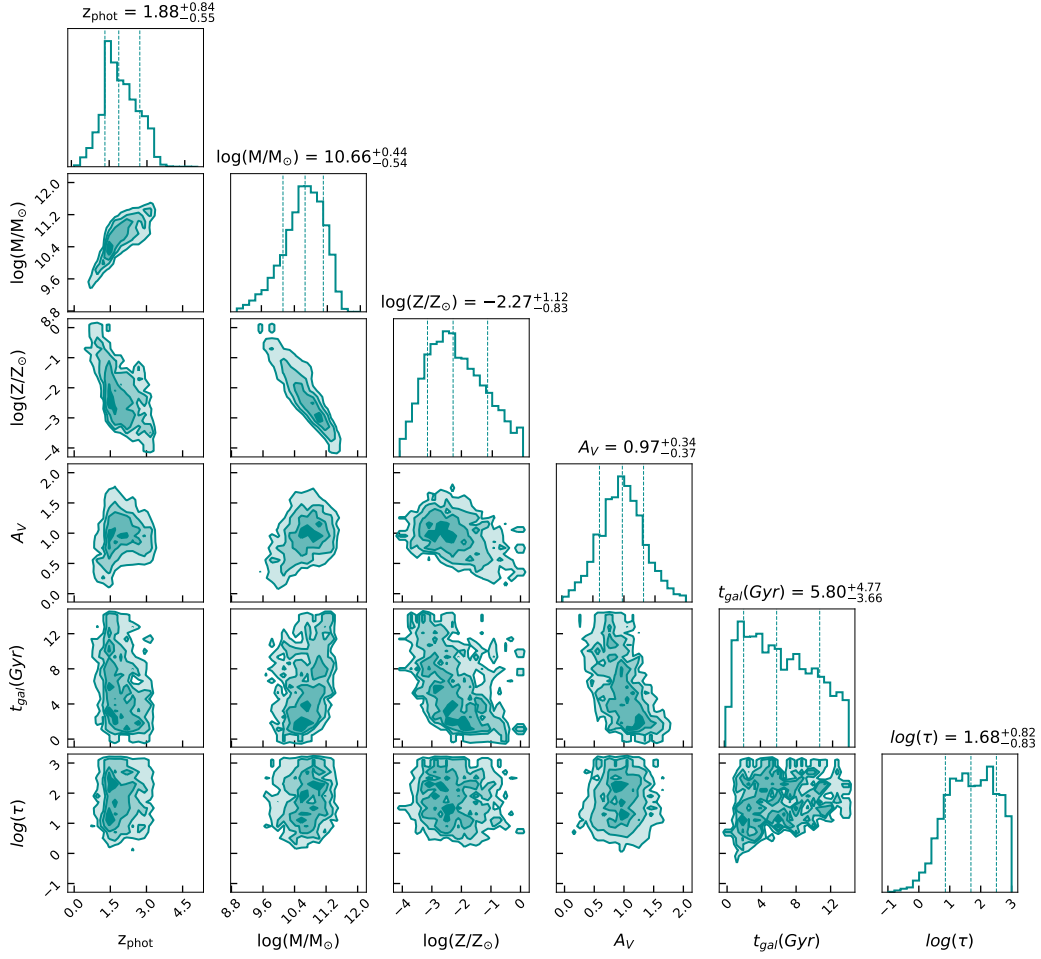
**Fig. A.2.** Posterior distributions for the SED model parameters of the potential host galaxy of GRB 150309A. The distributions were obtained using nested sampling via `dynesty` in the `Prospector` software.